ACS APPLIED MATERIALS & INTERFACES

Research Article

www.acsami.org

Investigating the Mechanism of Reversible Lithium Insertion into Anti-NASICON $Fe_2(WO_4)_3$

Gözde Barim, Patrick Cottingham, Shiliang Zhou, Brent C. Melot,* and Richard L. Brutchey*

Department of Chemistry, University of Southern California, Los Angeles, California 90089, United States

Supporting Information

ABSTRACT: The gram-scale preparation of $Fe_2(WO_4)_3$ by a new solution-based route and detailed characterization of the material are presented. The resulting $Fe_2(WO_4)_3$ undergoes a reversible electrochemical reaction against lithium centered around 3.0 V with capacities near 93% of the theoretical maximum. Evolution of the $Fe_2(WO_4)_3$ structure upon lithium insertion and deinsertion is probed using a battery of characterization techniques, including in situ X-ray diffraction, neutron total scattering, and X-ray absorption spectroscopy (XAS). A structural transformation from monoclinic to orthorhombic phases is confirmed during lithium intercalation. XAS and neutron total scattering measurements verify that $Fe_2(WO_4)_3$ consists of trivalent iron and hexavalent tungsten ions. As lithium ions are inserted into the framework, iron ions are reduced to the divalent state, while the tungsten ions are electrochemically inactive and remain in the hexavalent state. Lithium insertion occurs via a concerted rotation of the rigid polyhedra in the host lattice driven by electrostatic interactions with the Li^+ ions; the magnitude of these polyhedral rotations was found to be slightly larger for $Fe_2(WO_4)_3$ than for the $Fe_2(MoO_4)_3$ analog.

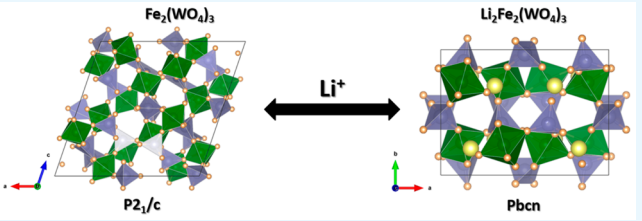

KEYWORDS: *battery, lithium ion, intercalation, NASICON, tungstate*

INTRODUCTION

Rechargeable Li-ion batteries have found utility in applications ranging from portable electronics to electric vehicles.[1−3] The majority of cathodes used in commercialized Li-ion batteries rely on layered lithium transition-metal oxides (i.e., $LiMO_2$, where M = Co, Mn, and Ni).[4,5] In oxides, the distortions that occur as Li^+ ions are intercalated into the lattice can induce severe changes in the structural framework leading to capacity fade over time. Therefore, a great deal of research has focused on the search for alternative cathode materials with better longevity, such as polyanion materials whose structural building blocks are comprised of corner-sharing polyhedral subunits. Since the first reports by Goodenough and co-workers, the structural and electrochemical properties of so-called polyanion compounds with rigid tetrahedral structural units (i.e., XO_4; X = S, P, Mo, etc.) have been extensively investigated.[6,7] These polyanion compounds exhibit better thermal stability when compared to layered lithium transition-metal oxides owing to the covalent X−O bonds in the tetrahedral subunits. Moreover, the redox potential of polyanion compounds can be tuned via polyanion substitution by modification of the ionic character of the M−O bond, which is known as the inductive effect.[8,9] NASICON-type frameworks were some of the initial polyanion compounds explored as cathodes in Li-ion batteries.[10−14] These materials are structurally comprised of covalently bonded 3D frameworks. The number of inserted alkali ions per formula unit depends on the available oxidation states of the element (X) in the tetrahedra and the transition metal (M) in the octahedra.[9,15]

Anti-NASICON-type $Fe_2(MO_4)_3$ (where M = Mo or W) is an interesting intercalation electrode material owing to the robust structural topology created by large interstitial voids scattered throughout a 3D network of polyhedra. The intercalation of monovalent ions into the Mo analog has been previously studied in some detail.[14,16−18] Recently, we reported the mechanistic difference between Li^+ and Na^+ insertion and deinsertion into the monoclinic polymorph of $Fe_2(MoO_4)_3$. It was found that sufficient Li^+ intercalation produces a phase transformation to a monoclinic structure featuring ordered Li^+ positions. This transformation proceeds via the concerted rotations of the tetrahedral and octahedral subunits, which is propelled by strong electrostatic interactions with the Li^+ ions. While Na^+ intercalation occurs in a fundamentally similar manner, sodium insertion results in a more incoherent structure because of its substantially larger ionic radius.[19] In contrast to $Fe_2(MoO_4)_3$, the structural and electrochemical properties of $Fe_2(WO_4)_3$ remain largely unexplored. This is possibly because the theoretical specific capacity (63 mA h g^{-1}) is much lower for this material owing to the heavy mass of tungsten. However, the excellent electrochemical cycling performance of this material, resulting from its extremely robust structural topology, makes it a fundamentally interesting material in which to study the mechanism of lithium intercalation.

Received: December 18, 2016
Accepted: March 7, 2017
Published: March 7, 2017

DOI: 10.1021/acsami.6b16216
ACS Appl. Mater. Interfaces 2017, 9, 10813−10819

Ferric tungstate was first reported in 1965 as a compound of unknown structure that was purported to melt at 1065 °C.[20] Subsequently, Pernicone and Fagherazzi prepared a phase-impure mixture of "$Fe_2W_3O_{12}$" and WO_3 through a precipitation method followed by annealing at 700 °C under flowing oxygen, and identified the new iron tungstate as having a tetragonal unit cell.[21] In 1985, Harrison et al. were the first to successfully prepare true $Fe_2(WO_4)_3$ and reported it to be isostructural with $Fe_2(MoO_4)_3$ and crystallize in a monoclinic ($P2_1/a$) space group.[22] Sriraman and Tyahi confirmed this assignment and reported the thermal decomposition of $Fe_2(WO_4)_3$ to $FeWO_4$ and WO_3 at temperatures above 750 °C.[23] Monoclinic $Fe_2(WO_4)_3$ crystallizes into a 3D structure consisting of corner-sharing FeO_6 octahedra and WO_4 tetrahedra.[22] In contrast to the isostructural $Fe_2(MoO_4)_3$, the tungstate congener does not have a high-temperature orthorhombic polymorph.[23] To date, the structural aspects of lithium intercalation into $Fe_2(WO_4)_3$ have only been investigated by Goodenough and co-worker through chemical insertion with ex situ powder X-ray diffraction (XRD).[24] They showed that chemical Li^+ insertion into $Fe_2(WO_4)_3$ results in a fully lithiated $Li_2Fe_2(WO_4)_3$ phase that crystallizes into a structure indexed to an orthorhombic ($Pbcn$) space group in the same way as the molybdate. Up to this point, detailed structural characterization of anti-NASICON $Fe_2(WO_4)_3$, the mechanism through which Li^+ ions electrochemically (de)insert into the material, and how the structural evolution is correlated with electrochemical cycling, has not been reported. Herein, we report a gram-scale solution precipitation synthesis of phase-pure anti-NASICON $Fe_2(WO_4)_3$. We investigate the structural transformation of the pristine material into the orthorhombic lithiated $Li_2Fe_2(WO_4)_3$ phase via intercalation, and demonstrate the correlation between structural evolution and electrochemical properties of $Fe_2(WO_4)_3$.

EXPERIMENTAL SECTION

Synthesis. $Fe_2(WO_4)_3$ was prepared under ambient conditions. Ammonium paratungstate hydrate [$(NH_4)_{10}W_{12}O_{41}{\cdot}xH_2O$, 0.58 mmol] from Alfa Aesar and iron(III) nitrate hydrate [$Fe(NO_3)_3{\cdot}9H_2O$, 4.65 mmol] from Sigma Aldrich (St. Louis) were individually dissolved in 150 and 50 mL of deionized water, respectively. $NH_3{\cdot}H_2O$ (0.5 mL) was then added dropwise to the paratungstate solution. The aqueous solution of $Fe(NO_3)_3$ was then added dropwise to the basic paratungstate solution with rapid stirring, which yields an orange precipitate. The solution was subsequently stirred for 12 h. The orange precipitate was filtered and subsequently washed with ethanol two times. The powder was dried under vacuum for 5 h at 60 °C. The resulting powder was ground and heated at 475 °C for 8 h in air, resulting in a brownish-orange powder. This powder was subsequently heated at 550 °C for 8 h in air, resulting in a crystalline, light orange $Fe_2(WO_4)_3$ powder in 95% isolated ceramic yield by the following reaction: $8Fe(NO_3)_3{\cdot}9H_2O + (NH_4)_{10}W_{12}O_{41}{\cdot}xH_2O \rightarrow 4Fe_2(WO_4)_3 + 34NH_3 + 48O_2 + (41 + x)H_2O$.

Chemical Insertion. The chemical lithiation of $Fe_2(WO_4)_3$ was achieved by stirring 1.0 g of $Fe_2(WO_4)_3$ with 10 mol equiv of LiI for 2 weeks in dry acetonitrile inside a glove box filled with ultrapure Ar. The resulting light brown material was washed twice with dry acetone in the glove box. The final material was dried under vacuum overnight at room temperature.

Powder X-ray Diffraction (XRD). Laboratory XRD was performed using a Co Kα source (λ_1 = 1.78897 Å, λ_2 = 1.79285 Å) in a Bruker D8 diffractometer with LynxEye detector. Data was collected using the same conditions for each sample, including a step size of 0.02° 2θ, a 0.6 mm slit, and a 1 h collection time for the range of 10° < 2θ < 60°. The electrochemical cell used for in situ XRD has been described elsewhere.[25]

Transmission Electron Microscopy (TEM). TEM was performed on a JEOL JEM2100F (JEOL Ltd.) with an operating voltage of 200 kV. Samples for TEM analysis were prepared by drop-casting a suspension of the powder in ethanol onto a 200 mesh Cu grid coated with a lacey carbon film (Ted Pella, Inc., Redding, CA).

Electrochemical Measurements. Electrochemical measurements were performed in Swagelok-type cells, the details of which have been reported elsewhere.[25] In short, the positive electrodes were made by mixing Ketjen black carbon and $Fe_2(WO_4)_3$ (1:2 w/w) for 30 min in a glove box filled with ultrapure Ar. A Li-metal disk was used as the negative electrode, and borosilicate glass fiber sheets (Whatman GF/D) were utilized as the separator. The electrolyte solution was comprised of 1 M $LiPF_6$ in dimethylene carbonate and ethylene carbonate (1:1 w/w). The electrochemical cells were prepared by grinding ca. 8 mg of active material with Ketjen black carbon and cycled at room temperature between 2.4 and 3.8 V versus Li at a rate of C/10. Galvanostatic cycling was performed on a BioLogic VMP3 potentiostat.

X-ray Absorption Near-Edge Structure (XANES). The 20-BM-B line at Argonne National Laboratory was used to collect XANES spectra. Fe K-edge and W L_{III}-edge XAS were collected in transmission mode using N_2-filled gas ionization chambers to monitor the incident and transmitted intensities. Samples for XANES were prepared by depositing a thin layer of the powder on Kapton tape. The incident X-ray beam size was between 1 and 6 mm (unfocused), and the spectra were collected under flowing He. The spectra were normalized by subtracting the pre-edge and applying an edge-jump normalization using the Athena software package.[26]

Pair Distribution Function (PDF). Room-temperature neutron total scattering was performed on well-ground polycrystalline samples packed in vanadium sample containers using the Nanoscale-Ordered Materials Diffractometer (NOMAD, BL-1B) instrument at the Spallation Neutron Source, Oak Ridge National Laboratory. Data were collected for 40 min per sample over the range of 3° < 2θ < 175°. Custom software developed by ORNL was used to produce $S(Q)$, a reduced scattering function in which contributions from the sample holder and vanadium can were subtracted. $G(r)$, the PDF, was obtained by Fourier transformation of $S(Q)$ with a Q_{max} of ~32 Å^{-1}. Fits to the resulting PDFs were performed in PDFgui.[27]

Symmetry-Mode Analysis. The AMPLIMODES software available from the Bilbao Crystallographic Server was used to perform symmetry-mode analysis.[28] The structural parameters of the low-symmetry pristine structure and high-symmetry lithiated structure are input into the program. Results from PDF analysis of neutron total scattering data for $Fe_2(WO_4)_3$ and $Li_2Fe_2(WO_4)_3$ were used for the structural parameters for the low-symmetry and high-symmetry phases, respectively. For direct comparison, lithium atoms in the Li-inserted $Fe_2(WO_4)_3$ were left out in this analysis.

X-ray Photoelectron Spectroscopy (XPS). High-resolution spectra were collected on a Kratos Axis Ultra XPS with the analyzer lens in hybrid mode. An operating current of 6 mA and voltage of 10 kV were applied using a monochromatic aluminum electrode. A step size of 0.1 eV and a pass energy of 20 eV were used, and pressure was maintained around 1−3 × 10^{-8} Torr. Binding energies were referenced to C 1s at 284 eV. Samples were prepared by pressing ~75 mg of dry powder into 13-mm-diameter pellets using ~5 t of pressure for 3 min and applying the pellets onto conductive carbon tape.

Gas Sorption Analysis. Brunauer−Emmett−Teller (BET) was collected using a Nova 2200e surface area and pore size analyzer (Quantachrome Instruments, Inc.). Materials were degassed for 2 h at 150 °C in vacuo before measurement.

Elemental Analysis. Samples were sent to Galbraith Laboratories, Inc. for inductively coupled plasma optical emission spectroscopy (ICP-OES) to assess Fe, W, and Li content.

RESULTS AND DISCUSSION

Attempts to prepare $Fe_2(WO_4)_3$ through a high-temperature solid-state route were first reported by Nassau et al., but were

DOI: 10.1021/acsami.6b16216
ACS Appl. Mater. Interfaces 2017, 9, 10813−10819

found to be unsuccessful.[20] Following this work, there have been a handful of successful examples of lower-temperature synthesis of monoclinic $Fe_2(WO_4)_3$ through solution-based precipitation methods.[22,23] The difficulty in preparing phase-pure monoclinic $Fe_2(WO_4)_3$ arises from its thermal instability at high temperatures, with traditional solid-state routes leading to the formation of the thermodynamically stable $FeWO_4$ phase via disproportionation.[20,23] Previous routes to monoclinic $Fe_2(WO_4)_3$ using solution precipitation methods relied on the use of a Na_2WO_4 precursor, which can lead to sodium-inserted products.[22] Therefore, we developed an alternative precipitation approach using $(NH_4)_{10}W_{12}O_{41}{\cdot}xH_2O$ and $Fe(NO_3)_3{\cdot}9H_2O$ as the starting materials. This method relies on the room-temperature precipitation of an amorphous nanoparticulate product with subsequent two-stage thermal annealing. The washed and dried amorphous nanoparticles are first heated to 475 °C for 8 h, followed by an additional annealing step at 550 °C for 8 h. This graded annealing provides better crystallinity than direct thermal aging of the amorphous product at 550 °C for 8 h (Supporting Information, Figure S1). Direct thermal annealing at 600 °C or thermal annealing above 650 °C results in the decomposition of $Fe_2(WO_4)_3$ into $FeWO_4$ and WO_3 instead of a phase transition from the monoclinic phase into a high-temperature orthorhombic phase, as is the case for the molybdate.[23] This synthetic approach results in the preparation of large quantities of phase-pure $Fe_2(WO_4)_3$, with isolated ceramic yields of 95%.

The phase purity and crystal structure of the pristine, monoclinic $Fe_2(WO_4)_3$ was confirmed by neutron total scattering data acquired using the NOMAD instrument at Oak Ridge National Laboratory. Modeling was constrained to the ($P2_1/c$) space group for monoclinic $Fe_2(MoO_4)_3$ and initialized with structural parameters reported by Chen.[29] The fit to the experimental PDF of monoclinic $Fe_2(WO_4)_3$ in the 1.6−15 Å range is shown in Figure 1. Results of the fit (i.e., cell parameters, atomic positions, and isotropic displacement parameters) are provided in the Supporting Information (Table S1). The low value of R_w, as well as visual inspection of the fit to the experimental data, confirm that $Fe_2(WO_4)_3$ is isostructural with $Fe_2(MoO_4)_3$ and that the structure is well-described by the monoclinic ($P2_1/c$) anti-NASICON structure (Figure 1b).

The chemical composition of the pristine $Fe_2(WO_4)_3$ was determined by ICP-OES to possess a Fe/W ratio of 0.65, in close agreement with the nominal composition of the material. To further probe the composition of the pristine material, X-ray photoelectron spectroscopy (XPS) was used. Binding energies of 711.3 and 35.6 eV were observed for Fe $2p_{3/2}$ and W $4f_{7/2}$, respectively, with spin−orbit splitting matching closely with literature values for Fe^{3+} and W^{6+}.[30,31] Additionally, a broad peak at 41.5 eV corresponds to the expected W 5p binding energy for W^{6+} (see Supporting Information, Figure S2). Transmission electron microscopy (TEM) was used to gain insight into the morphology of the resulting monoclinic $Fe_2(WO_4)_3$ (Figure 2). TEM images before and after annealing to 550 °C reveal that thermal treatment leads to the aggregation and grain growth of the amorphous nanoparticles, with an increase in primary particle size from ∼50 to ∼200 nm being observed. The corresponding BET surface area of $Fe_2(WO_4)_3$ after annealing was 13 $m^2\ g^{-1}$ by nitrogen adsorption (Supporting Information, Figure S3).

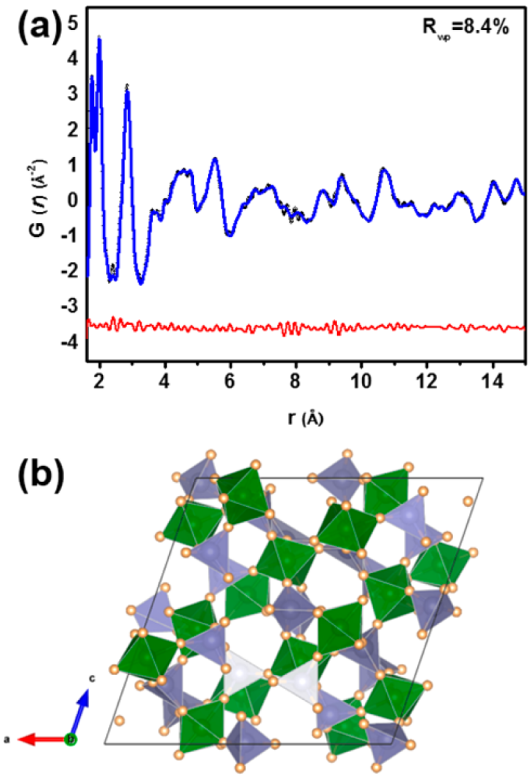

Figure 1. (a) Experimental PDF of pristine $Fe_2(WO_4)_3$ neutron total scattering data acquired using the NOMAD instrument at Oak Ridge National Laboratory and a refined model fit based on the monoclinic structure; (b) the resulting crystal structure. (Iron, tungsten, and oxygen are shown as green, purple, and orange, respectively.)

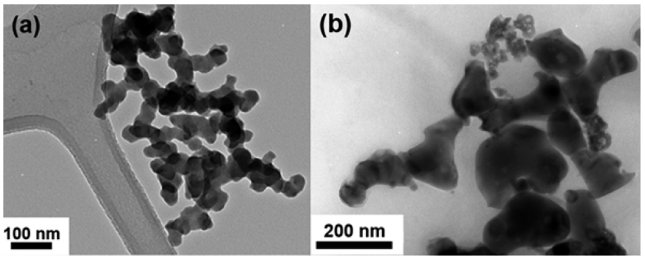

Figure 2. TEM images of $Fe_2(WO_4)_3$ (a) before and (b) after annealing to 550 °C.

The electrochemical behavior of monoclininc $Fe_2(WO_4)_3$ toward Li^+ (de)insertion was investigated by galvanostatic cycling in concert with in situ X-ray diffraction. Figure 3a shows the first ten galvanostatic electrochemical cycles of $Fe_2(WO_4)_3$ against Li/Li^+ at a cycling rate of C/10. It was determined that 93% of the theoretical maximum of two Li^+ ions per $Fe_2(WO_4)_3$ was achieved on the first discharge. The first derivative of the galvanostatic cycling curve gives two peaks at 3.01 and 2.96 V during oxidation and reduction, respectively (Figure 3b). The small degree of polarization suggests an excellent reversibility of lithium (de)insertion into the anti-NASICON framework operating on the Fe^{3+}/Fe^{2+} redox couple. Even though the cell assembly had not been rigorously optimized, the capacity retention of the cells was around 95% after 25 cycles at a galvanostatic cycling rate of C/10 (see Supporting Information, Figure S4). The voltage−composition curve possesses a single plateau during Li^+ insertion and deinsertion, which is suggestive of a two-phase

DOI: 10.1021/acsami.6b16216
ACS Appl. Mater. Interfaces 2017, 9, 10813−10819

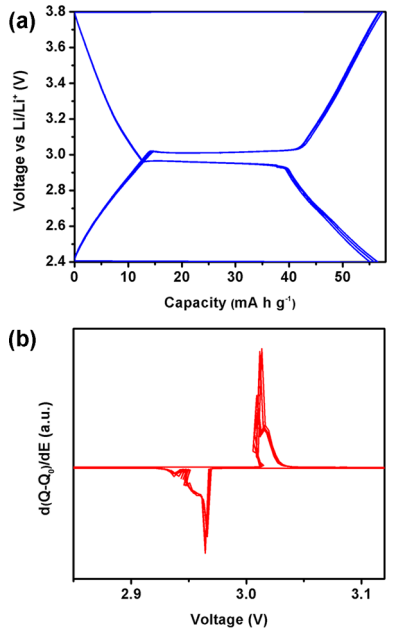

Figure 3. (a) Galvanostatic electrochemical cycling of $Fe_2(WO_4)_3$ against Li^+ intercalation and (b) its derivative curve.

intercalation process where the lithiated phase forms directly in increasing mass fraction with increasing lithium content, as opposed to a continuous solid-solution process.[24,32]

To confirm that lithium (de)insertion is occurring through a two-phase process, conversion of the monoclinic $Fe_2(WO_4)_3$ structure upon lithium insertion and deinsertion was monitored by in situ X-ray diffraction. A heat map of in situ XRD patterns taken during electrochemical cycling at a rate of C/10 is shown in Figure 4. The *y*-axis corresponds to inserted and extracted

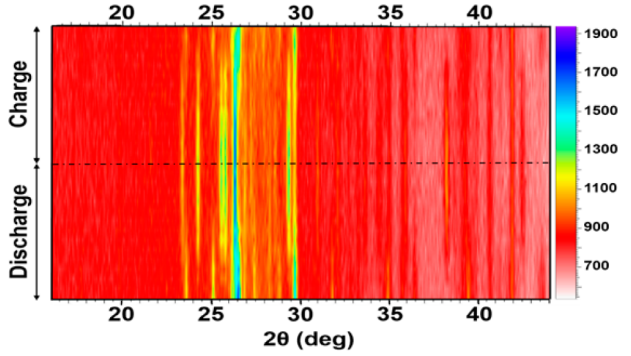

Figure 4. 2D pattern of in situ XRD study for a full discharge/charge cycle of $Fe_2(WO_4)_3$ against lithium at C/10 rate using a Co Kα source (λ_1 = 1.78897 Å, λ_2 = 1.79285 Å). Color indicates the intensities of reflections.

lithium content upon discharging and charging, respectively. The reflections of pristine, monoclinic $Fe_2(WO_4)_3$ gradually disappear without any shift in peak positions. For example, Figure 4 shows that the intensities of reflections at 25.1°, 26.6°, 31.8°, 34.9°, and 39.5° 2θ gradually decrease with increasing Li^+ content during discharging. This observation is characteristic of a two-phase insertion process, with a new set of diffraction peaks (i.e., at 24.3°, 25.6°, 25.8°, 26.3°, 29.4°, 31.0°, 38.3°, and 42.5° 2θ) appearing upon discharging since the lithiated phase crystallizes into a different structure. This new lithium-inserted $Li_2Fe_2(WO_4)_3$ phase is indexed to an orthorhombic structure with a *Pbcn* space group, as originally posited by Goodenough and co-worker.[24] While charging, intensity changes were observed in reverse, demonstrating that the structural conversion is highly reversible with Li^+ insertion and deinsertion, as suggested by electrochemical cycling data (Figure 3). The coexistence of Bragg reflections associated with both $Fe_2(WO_4)_3$ and $Li_2Fe_2(WO_4)_3$ confirms the two-phase mechanism for the phase transformation.

While the structure of $Li_2Fe_2(WO_4)_3$ was previously postulated to be isostructural to $Li_2Fe_2(MoO_4)_3$,[24] we sought to verify this by chemically inserting Li^+ ions into $Fe_2(WO_4)_3$ by soaking powders in a solution of LiI in dry acetonitrile so that high-quality neutron total scattering data could be collected. The final stoichiometry of the lithiated phase was found to have a Li/Fe/W ratio of 0.72:0.66:1 by ICP-OES. The fit of the experimental PDF on the chemically lithiated phase in the 1.6−15 Å range is given in Figure 5a. The

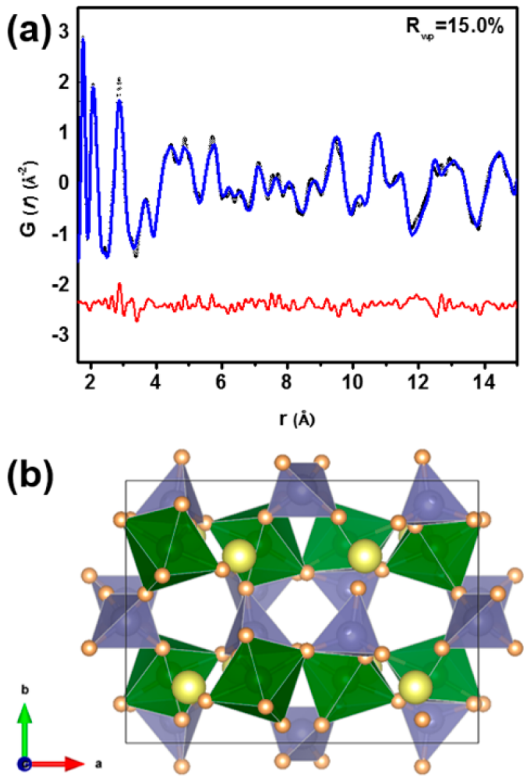

Figure 5. (a) The experimental PDF of lithium-inserted $Li_2Fe_2(WO_4)_3$ neutron total scattering data acquired using the NOMAD instrument at Oak Ridge National Laboratory, and a refined model fit based on the orthorhombic structure; (b) resulting crystal structure. (Iron, tungsten, oxygen, and lithium are shown as green, purple, orange, and yellow, respectively.)

experimental PDF of lithiated phase was modeled to the *Pbcn* space group using the structural parameters given by Manthiram et al. for $Li_2Fe_2(WO_4)_3$.[24,33] A high quality-of-fit was achieved with a low R_{wp} value of 15%. Results of the fit (i.e., cell parameters, atomic positions, and isotropic atomic displacement parameters) are provided in the Supporting Information, Table S2. The excellent fit of the PDF extracted from neutron total scattering data to the orthorhombic phase confirms that the fully lithiated anti-NASICON frameworks of $Li_2Fe_2(WO_4)_3$ and $Li_2Fe_2(MoO_4)_3$ are indeed isostructural (Figure 5b).

DOI: 10.1021/acsami.6b16216
ACS Appl. Mater. Interfaces 2017, 9, 10813−10819

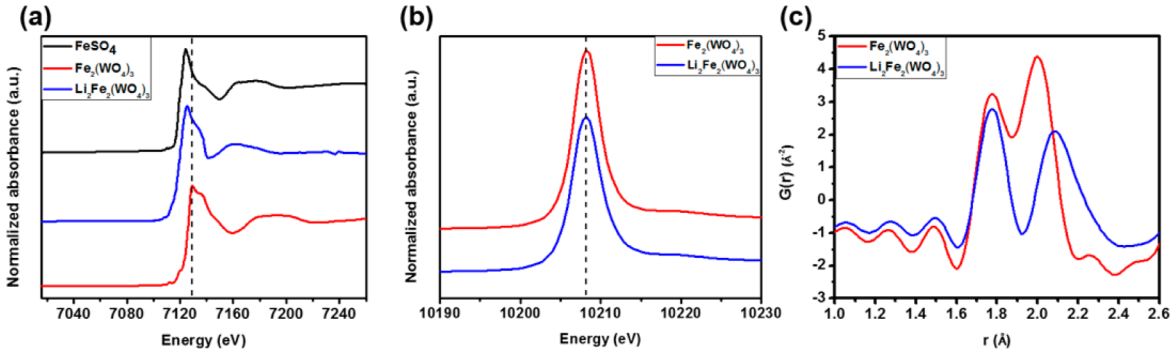

Figure 6. Normalized (a) Fe K-edge and (b) W L_{III}-edge XANES spectra, and (c) experimental neutron total scattering data for $Fe_2(WO_4)_3$ and chemically lithiated $Li_2Fe_2(WO_4)_3$.

Given that tungsten can adopt both a hexavalent and tetravalent oxidation state, we sought to interrogate whether the redox center associated with Li (de)insertion in $Fe_2(WO_4)_3$ is fully isolated to the iron ions in the structure. In this regard, X-ray absorption near-edge structure (XANES) spectroscopy has proven extremely useful for determining the oxidation state of metals in polyanion cathode materials.[34,35] XANES measurements were performed on $Fe_2(WO_4)_3$ before and after lithium intercalation. The Fe K-edge XANES spectra of the $Fe_2(WO_4)_3$ and $Li_2Fe_2(WO_4)_3$ samples compared against $FeSO_4$ are given in Figure 6a. The position of the absorption edge in pristine $Fe_2(WO_4)_3$ (i.e., 7124.9 eV) is shifted toward lower energy upon lithium intercalation, with the absorption edges of $Li_2Fe_2(WO_4)_3$ and $FeSO_4$ (i.e., 7119.2 and 7119.1 eV, respectively) being nearly identical and conforming to the change in iron oxidation state from 3+ to 2+ upon lithiation.[35] Potential variations in the electronic structure of the polyanion subunits before and after lithium intercalation were probed through W L_{III}-edge XANES spectroscopy. The XANES regions of W L_{III}-edge in $Fe_2(WO_4)_3$ and $Li_2Fe_2(WO_4)_3$ are given in Figure 6b. Both pristine and lithiated samples exhibit a characteristic sharp asymmetrical peak for tetrahedral W units, which are attributed to electron transitions from $2p_{3/2}$ to 5d states. These W L_{III} absorption edges of the pristine and lithiated phases are identical, indicating that lithium intercalation does not affect the electronic structure around tungsten.

The neutron total scattering data for $Fe_2(WO_4)_3$ and $Li_2Fe_2(WO_4)_3$ were compared to probe the intercalation mechanism at the local scale of the anti-NASICON framework. Experimental pair distribution functions of pristine and lithiated phases in the range of 1.0−2.6 Å are given in Figure 6c. The PDF peak at 1.77 Å corresponds to the W−O interatomic distance within the tungstate tetrahedra and is invariant with lithium intercalation, consistent with the rigidity of these polyhedral subunits. Conversely, the Fe−O interatomic distance increases from 2.00 to 2.09 Å after lithium intercalation into the framework, consistent with reduction of the Fe center from 3+ to 2+ on lithium insertion and in agreement with XANES analysis. Collectively, this confirms that lithium (de)insertion operates only on Fe^{3+}/Fe^{2+} redox couple.

To more rigorously describe the structural distortion of the monoclinic $Fe_2(WO_4)_3$ phase into orthorhombic phase, symmetry-mode analysis using the *AMPLIMODES* software from the Bilbao Crystallographic Server was performed.[28] The transformation of the low-symmetry $Fe_2(WO_4)_3$ structure into the higher-symmetry $Li_2Fe_2(WO_4)_3$ was identified by using a transformation matrix (see Supporting Information, Table S3). The higher-symmetry structure (*Pbcn*) was converted into the low-symmetry ($P2_1/c$) one after subtraction of lithium atoms from the lithiated structure, and then atoms in these two structures were directly paired (see Supporting Information, Table S4 and Table S5). The displacement vectors on each atom for the structural transformation are displayed in Figure 7,

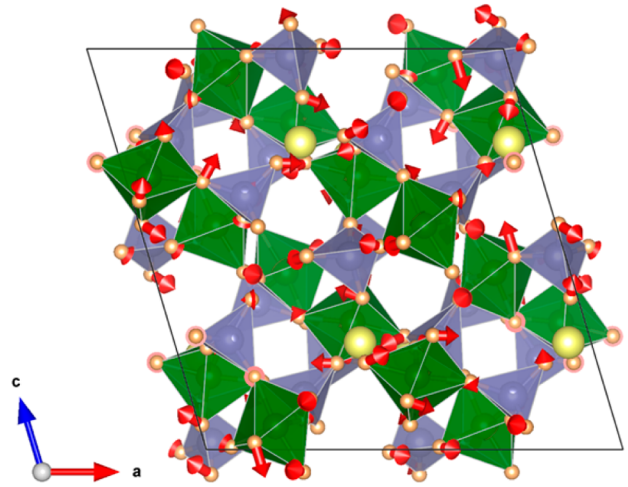

Figure 7. Transformation vectors on each atom from the symmetry-mode analysis between $Fe_2(WO_4)_3$ and $Li_2Fe_2(WO_4)_3$, with the atomic positions of Fe, W, and O in $Fe_2(WO_4)_3$ and the atomic position of lithium in $Li_2Fe_2(WO_4)_3$ converted into the same $P2_1/c$ reference structure. Li^+ ions were removed for the symmetry-mode analysis, but are included in the reference structure for clarity. (Iron, tungsten, oxygen, and lithium atoms are shown as green, purple, orange, and yellow, respectively.)

and a comprehensive list of precise vectors is provided in the Supporting Information, Table S6. The dominant distortions observed from the symmetry-mode analysis are displacements of the oxygen atoms. The corresponding displacement vectors for W and Fe atoms were found to be negligible, indicating that there is a preservation of center of mass of the polyhedral subunits during rotational distortions upon Li^+ insertion. In other words, the structural transformation during lithium intercalation into $Fe_2(WO_4)_3$ is driven by a rotational movement of oxygen atoms toward lithium, which likely stems from the creation of new electrostatic interactions with the framework. This type of analysis identifies changes to the periodic rotational symmetry of the unit cell, but it should be noted that short-range noncooperative distortions of the lattice that may also play a role in accomplishing the structural distortion cannot be captured using this approach.

DOI: 10.1021/acsami.6b16216
ACS Appl. Mater. Interfaces 2017, 9, 10813−10819

From this, we can draw some mechanistic comparisons between lithium (de)insertion into anti-NASICON-type $Fe_2(MO_4)_3$, where M = W or Mo. A discharge voltage of 2.96 V for $Fe_2(WO_4)_3$ is slightly lower than that of $Fe_2(MoO_4)_3$ (3.0 V), but is so close that the differences are most likely a result of polarization from differences in the processing of the cathode active material (i.e., efficiency of the carbon coating and particle morphology/size).[34] The plateau in the galvanostatic voltage−composition curves for both $Fe_2(WO_4)_3$ and $Fe_2(MoO_4)_3$ suggest a similar two-phase structural transformation on lithium (de)insertion, which was further corroborated by in situ X-ray diffraction experiments. As is the case for $Fe_2(MoO_4)_3$, we find reversible variations in the intensities of reflections during the (de)insertion of Li^+ into $Fe_2(WO_4)_3$, with no remarkable shifts in the positions of the Bragg reflections being observed. Both in situ XRD and galvanostatic electrochemical cycling experiments point toward a conversion of the monoclinic form into orthorhombic $Li_2Fe_2(WO_4)_3$ through a two-phase process. The structure of fully lithiated $Li_2Fe_2(WO_4)_3$ was also confirmed to be orthorhombic with a *Pbcn* space group through PDF analysis of neutron total scattering data on the chemically inserted material. This lithiated phase appears to be isostructural with that of $Li_2Fe_2(MoO_4)_3$. Since $Fe_2(WO_4)_3$ and $Fe_2(MoO_4)_3$ are isostructural for both the pristine and lithiated phases, with an identical structural topology with regards to polyhedral connectivity, we expect an analogous structural transformation mechanism for both materials.

We recently demonstrated that $Fe_2(MoO_4)_3$ undergoes a transformation into the orthorhombic phase via the cooperative rotation of rigid tetrahedral subunits as Li^+ is inserted.[19] More specifically, the molybdate tetrahedra maintained a rigid Mo−O bond length, but were found to pivot around their crystallographic position so that the oxygen ions could displace toward the new position of the Li^+ ions. The symmetry-mode analysis of the transformations are nearly identical for both $Fe_2(WO_4)_3$ and $Fe_2(MoO_4)_3$, as might be expected from the similar ionic radii of four-coordinate, hexavalent Mo and W atoms (0.42 and 0.41 Å, respectively);[36] however, the magnitude of the total distortion was found to be slightly larger for $Fe_2(WO_4)_3$. The amplitude of the global distortion, which represents a sum of the displacement for all atoms in the unit cell, for $Fe_2(WO_4)_3$ and $Fe_2(MoO_4)_3$, were determined to be 6.50 and 6.17 Å, respectively. This difference most likely arises from differences in the bonding within the two tetrahedral subunits. Tungsten has a Pauling electronegativity of 2.36, compared to molybdenum, which is 2.16.[37] This suggests that the tungstate tetrahedra should be more covalent, and through inductive effects should increase the iconicity of the Fe−O bonds. As a result, it should be easier to distort the Fe−O bonds away from ideal, facilitating a more pronounced magnitude in the rotational distortion as observed.

CONCLUSION

We have presented a new solution-based precipitation method for the gram-scale synthesis of anti-NASICON monoclinic $Fe_2(WO_4)_3$. Using a combination of structural and electrochemical probes, we have demonstrated the reversible (de)insertion of lithium into the $Fe_2(WO_4)_3$ framework. Galvanostatic cycling indicates that $Fe_2(WO_4)_3$ undergoes a reversible electrochemical reaction centered around ∼3.0 V with a remarkable capacity retention of 95% over 25 cycles at a C/10 cycling rate. XANES and neutron total scattering studies confirm that the charge compensation upon Li^+ (de)insertion is achieved through the Fe^{3+}/Fe^{2+} redox couple only. A two-phase lithium intercalation process was established by in situ XRD, and transformation of the initial monoclinic structure into an orthorhombic lithiated structure was demonstrated by symmetry-mode analysis to proceed through the filling of defined crystallographic positions by inserted lithium atoms via cooperative rotations of polyhedral subunits. This comprehensive study provides constructive information on the electrochemical performance and structural evolution of NASICON-type materials, which may facilitate further development of insertion cathodes for rechargeable Li-ion batteries.

ASSOCIATED CONTENT

Supporting Information

The Supporting Information is available free of charge on the ACS Publications website at DOI: 10.1021/acsami.6b16216.

Additional experimental details, XRD patterns of $Fe_2(WO_4)_3$ at different annealing temperatures, XPS spectra and gas sorption analysis of $Fe_2(WO_4)_3$, capacity retention of batteries, results of PDF analysis of experimental neutron total scattering data on pristine and lithiated $Fe_2(WO_4)_3$, detailed symmetry-mode analysis results of $Fe_2(WO_4)_3$, and structural evolution of $Fe_2(WO_4)_3$ upon Li intercalation (PDF)

AUTHOR INFORMATION

Corresponding Authors

*E-mail: brutchey@usc.edu.

*E-mail: melot@usc.edu

ORCID

Richard L. Brutchey: 0000-0002-7781-5596

Notes

The authors declare no competing financial interest.

ACKNOWLEDGMENTS

G.B., P.C., and R.L.B. acknowledge the Department of Energy Office of Basic Energy Sciences under Grant No. DE-FG02-11ER46826 for funding the synthesis and structural characterization. B.C.M. acknowledges support through a CAREER award from the National Science Foundation under Grant No. DMR-1554204 for the electrochemical studies. B.C.M also acknowledges Research Corporation for Science Advancement for a Cottrell Scholar award. Use of the Advanced Photon Source at Argonne National Laboratory was supported by the U.S. Department of Energy, Office of Science, Office of Basic Energy Sciences, under Contract No. DE-AC02-06CH11357. Neutron diffraction studies were supported by the Office of Basic Energy Sciences, U.S. Department of Energy, at the Spallation Neutron Source, Oak Ridge National Laboratory, under Contract No. DEAC05-00OR22725 with UT Battelle.

REFERENCES

(1) Etacheri, V.; Marom, R.; Elazari, R.; Salitra, G.; Aurbach, D. Challenges in the Development of Advanced Li-ion Batteries: A review. *Energy Environ. Sci.* **2011**, *4*, 3243−3262.

(2) Lu, L.; Han, X.; Li, J.; Hua, J.; Ouyang, M. A Review on the Key Issues for Lithium-ion Battery Management in Electric Vehicles. *J. Power Sources* **2013**, *226*, 272−288.

(3) Andre, D.; Kim, S.-J.; Lamp, P.; Lux, S. F.; Maglia, F.; Paschos, O.; Stiaszny, B. Future Generations of Cathode Materials: an

Automotive Industry Perspective. *J. Mater. Chem. A* **2015**, *3*, 6709−6732.
(4) Mizushima, K.; Jones, P. C.; Wiseman, P. J.; Goodenough, J. B. Li_xCoO_2 (0< x<-1): A New Cathode Material for Batteries of High Energy Density. *Mater. Res. Bull.* **1980**, *15*, 783−789.
(5) Armstrong, A. R.; Bruce, P. G. Synthesis of Layered $LiMnO_2$ as an Electrode for Rechargeable Lithium Batteries. *Nature* **1996**, *381*, 499−500.
(6) Padhi, A. K. Mapping of Transition Metal Redox Energies in Phosphates with NASICON Structure by Lithium Intercalation. *J. Electrochem. Soc.* **1997**, *144*, 2581.
(7) Nanjundaswamy, K. S.; Padhi, A. K.; Goodenough, J. B.; Okada, S.; Ohtsuka, H.; Arai, H.; Yamaki, J. Synthesis, Redox Potential Evaluation and Electrochemical Characteristics of NASICON-related-3D Framework Compounds. *Solid State Ionics* **1996**, *92*, 1−10.
(8) Masquelier, C.; Croguennec, L. Polyanionic (phosphates, silicates, sulfates) Frameworks as Electrode Materials for Rechargeable Li (or Na) Batteries. *Chem. Rev.* **2013**, *113*, 6552−6591.
(9) Padhi, A. K.; Manivannan, V.; Goodenough, J. B. Tuning the Position of the Redox Couples in Materials with NASICON Structure by Anionic Substitution. *J. Electrochem. Soc.* **1998**, *145*, 1518−1520.
(10) Anantharamulu, N.; Koteswara Rao, K.; Rambabu, G.; Vijaya Kumar, B.; Radha, V.; Vithal, M. A Wide-ranging Review on NASICON type Materials. *J. Mater. Sci.* **2011**, *46*, 2821−2837.
(11) Vijayan, L.; Govindaraj, G. NASICON Materials: Structure and Electrical Properties. In *Polycrystalline Materials - Theoretical and Practical Aspects*; Zakhariev, Z., Ed.; InTech: Rijeka, Croatia,2012; p 77.
(12) Masquelier, C.; Padhi, A. K.; Nanjundaswamy, K. S.; Goodenough, J. B. New Cathode Materials for Rechargeable Lithium Batteries: The 3-D Framework Structures $Li_3Fe_2(XO_4)_3$ (X = P, As). *J. Solid State Chem.* **1998**, *135*, 228−234.
(13) Masquelier, C.; Wurm, C.; Rodriguez-Carvajal, J.; Gaubicher, J.; Nazar, L. A Powder Neutron Diffraction Investigation of the Two Rhombohedral NASICON Analogues: γ-$Na_3Fe_2(PO4)_3$ and $Li_3Fe_2(PO_4)_3$. *Chem. Mater.* **2000**, *12*, 525−532.
(14) Torardi, C. C.; Prince, E. Structure of the Lithium Insertion Compound $Li_2Fe_2(MoO_4)_3$ from Neutron Powder Diffraction Data. *Mater. Res. Bull.* **1986**, *21*, 719−726.
(15) Nanjundaswamy, K. S.; Padhi, A. K.; Goodenough, J. B.; Okada, S.; Ohtsuka, H.; Arai, H.; Yamaki, J. Synthesis, Redox Potential Evaluation and Electrochemical Characteristics of NASICON-related-3D Framework Compounds. *Solid State Ionics* **1996**, *92*, 1−10.
(16) Sun, Q.; Ren, Q.-Q.; Fu, Z.-W. NASICON-type $Fe_2(MoO_4)_3$ Thin Film as Cathode for Rechargeable Sodium Ion Battery. *Electrochem. Commun.* **2012**, *23*, 145−148.
(17) Nguyen, V.; Liu, Y.; Yang, X.; Chen, W. $Fe_2(MoO_4)_3$/Nanosilver Composite as a Cathode for Sodium-Ion Batteries. *ECS Electrochem. Lett.* **2015**, *4*, A29−A32.
(18) Yue, J.-L.; Zhou, Y.-N.; Shi, S.-Q.; Shadike, Z.; Huang, X.-Q.; Luo, J.; Yang, Z.-Z.; Li, H.; Gu, L.; Yang, X.-Q.; Fu, Z.-W. Discrete Li-occupation versus Pseudo-continuous Na-occupation and Their Relationship with Structural Change Behaviors in $Fe_2(MoO_4)_3$. *Sci. Rep.* **2015**, *5*, 8810.
(19) Zhou, S.; Barim, G.; Morgan, B. J.; Melot, B. C.; Brutchey, R. L. Influence of Rotational Distortions on Li^+- and Na^+-Intercalation in Anti-NASICON $Fe_2(MoO_4)_3$. *Chem. Mater.* **2016**, *28*, 4492−4500.
(20) Nassau, K.; Levinstein, H. J.; Loiacono, G. M. A Comprehensive Study of Trivalent Tungstates and Molybdates of the Type $L_2(MO_4)_3$. *J. Phys. Chem. Solids* **1965**, *26*, 1805−1816.
(21) Pernicone, N.; Fagherazzi, G. A New Iron Tungstate: $Fe_2W_3O_{12}$. *J. Inorg. Nucl. Chem.* **1969**, *31*, 3323−3324.
(22) Harrison, W. T. A.; Chowdhry, U.; Machiels, C. J. Preparation of Ferric Tungstate toward Methanol and Its Catalytic Behavior toward Methanol. *J. Solid State Chem.* **1985**, *60*, 101−106.
(23) Sriraman, A. K.; Tyagi, A. K. A New Method of $Fe_2(WO_4)_3$ Preparation and Its Thermal Stability. *Thermochim. Acta* **2003**, *406*, 29−33.
(24) Manthiram, A.; Goodenough, J. B. Lithium Insertion into $Fe_2(MO_4)_3$ Frameworks: Comparison of M = W with M = Mo. *J. Solid State Chem.* **1987**, *71*, 349−360.
(25) Cañas, N. A.; Hirose, K.; Pascucci, B.; Wagner, N.; Friedrich, K. A.; Hiesgen, R. Investigations of Lithium−sulfur Batteries using Electrochemical Impedance Spectroscopy. *Electrochim. Acta* **2013**, *97*, 42−51.
(26) Ravel, B.; Newville, M. ATHENA, ARTEMIS, HEPHAESTUS: Data Analysis for X-ray Absorption Spectroscopy using IFEFFIT. *J. Synchrotron Radiat.* **2005**, *12*, 537−541.
(27) Farrow, C. L.; Juhas, P.; Liu, J. W.; Bryndin, D.; Božin, E. S.; Bloch, J.; Proffen, T.; Billinge, S. J. L. PDFfit2 and PDFgui: Computer Programs for Studying Nanostructure in Crystals. *J. Phys.: Condens. Matter* **2007**, *19*, 335219.
(28) Orobengoa, D.; Capillas, C.; Aroyo, M. I.; Perez-Mato, J. M. AMPLIMODES: Symmetry-mode Analysis on the Bilbao Crystallographic Server. *J. Appl. Crystallogr.* **2009**, *42*, 820−833.
(29) Chen, H. The Crystal Structure and Twinning Behavior of Ferric Molybdate, $Fe_2(MoO_4)_3$. *Mater. Res. Bull.* **1979**, *14*, 1583−1590.
(30) McIntyre, N. S.; Zetaruk, D. G. X-ray Photoelectron Spectroscopic Studies of Iron Oxides. *Anal. Chem.* **1977**, *49*, 1521−1529.
(31) Kerkhof, F.; Moulijn, J. A.; Heeres, A. The XPS Spectra of the Metathesis Catalyst Tungsten Oxide on Silica Gel. *J. Electron Spectrosc. Relat. Phenom.* **1978**, *14*, 453−466.
(32) Levi, M. D.; Gamolsky, K.; Aurbach, D.; Heider, U.; Oesten, R. Determination of the Li ion Chemical Diffusion Coefficient for the Topotactic Solid-state Reactions Occurring via a Two-phase or Single-phase Solid Solution Pathway. *J. Electroanal. Chem.* **1999**, *477*, 32−40.
(33) α-$Li_2Fe_2(WO_4)_3$ ($Li_2Fe_2[WO_4]_3$ m) Crystal Structure: Datasheet from "PAULING FILE Multinaries Edition"; SpringerMaterials; Springer-Verlag, Berlin, Germany; Material Phases Data System (MPDS), Switzerland; and National Institute for Materials Science (NIMS), Japan, 2012.
(34) Barpanda, P.; Ati, M.; Melot, B. C.; Rousse, G.; Chotard, J.-N.; Doublet, M.-L.; Sougrati, M. T.; Corr, S. a.; Jumas, J.-C.; Tarascon, J.-M. A 3.90 V iron-based Fluorosulphate Material for Lithium-ion Batteries Crystallizing in the Triplite Structure. *Nat. Mater.* **2011**, *10*, 772−779.
(35) Shirakawa, J.; Nakayama, M.; Wakihara, M.; Uchimoto, Y. Changes in Electronic Structure upon Lithium Insertion into $Fe_2(SO_4)_3$ and $Fe_2(MoO_4)_3$ Investigated by X-ray Absorption Spectroscopy. *J. Phys. Chem. B* **2007**, *111*, 1424−1430.
(36) Shannon, R. D. T. Revised Effective Ionic Radii and Systematic Studies of Interatomic Distances in Halides and Chalcogenides. *Acta Crystallogr., Sect. A: Cryst. Phys., Diffr., Theor. Gen. Crystallogr.* **1976**, *32*, 751−767.
(37) Li, K.; Xue, D. Estimation of Electronegativity Values of Elements in Different Valence States. *J. Phys. Chem. A* **2006**, *110*, 11332−11337.

DOI: 10.1021/acsami.6b16216
ACS Appl. Mater. Interfaces 2017, 9, 10813−10819